

## Article

# An Ultrasensitive Laser-Induced Graphene Electrode-Based Triboelectric Sensor Utilizing Trapped Air as Effective Dielectric Layer

Tapas Kamilya <sup>1</sup>, Doohyun Han <sup>1</sup>, Jaehee Shin <sup>1</sup>, Soongeun Kwon <sup>2,\*</sup> and Jinhyoung Park <sup>1,\*</sup>

<sup>1</sup> Department of Mechatronics Engineering, Korea University of Technology & Education, 600, Chungjeol-ro, Byeongcheon-myeon, Dongnam-gu, Cheonan-si 31253, Republic of Korea; tkkt@koreatech.ac.kr (T.K.); hdh9903@koreatech.ac.kr (D.H.); wogmlchs@koreatech.ac.kr (J.S.)

<sup>2</sup> Nano-Convergence Manufacturing Systems Research Division, Korea Institute of Machinery & Materials, 156, Gajeongbuk-ro, Yuseong-gu, Daejeon 34103, Republic of Korea

\* Correspondence: sgkwon@kimm.re.kr (S.K.); jhpark98@koreatech.ac.kr (J.P.)

**Abstract:** Air, a widely recognized dielectric material, is employed as a dielectric layer in this study. We present a triboelectric sensor with a laser-induced graphene (LIG) electrode and an air-trapped pad using silicone rubber (SR). A very thin device with a thickness of 1 mm and an effective gap for contact–separation between the films of silicone rubber and polyimide (PI) of 0.6 mm makes the device extremely highly sensitive for very low amplitudes of pressure. The fabrication of LIG as an electrode material on the surface of PI is the key reason for the fabrication of the thin sensor. In this study, we showed that the fabricated air-trapped padded sensor (ATPS) has the capability to generate an output voltage of ~32 V, a short-circuit current of 1.2  $\mu$ A, and attain a maximum power density of 139.8  $\text{mW m}^{-2}$ . The performance of the ATPS was compared with a replicated device having a hole on the pad, allowing air to pass through during contact–separation. The observed degradation in the electrical output suggests that the trapped air in the pad plays a crucial role in enhancing the output voltage. Therefore, the ATPS emerges as an ultra-sensitive sensor for healthcare sensing applications.

**Keywords:** LIG; air-trapped pad; ATPS; silicone rubber; PI



**Citation:** Kamilya, T.; Han, D.; Shin, J.; Kwon, S.; Park, J. An Ultrasensitive Laser-Induced Graphene Electrode-Based Triboelectric Sensor Utilizing Trapped Air as Effective Dielectric Layer. *Polymers* **2024**, *16*, 26. <https://doi.org/10.3390/polym16010026>

Academic Editors: Fang-Chyow Chiu and Kartik Behera

Received: 21 November 2023

Revised: 7 December 2023

Accepted: 12 December 2023

Published: 20 December 2023



**Copyright:** © 2023 by the authors. Licensee MDPI, Basel, Switzerland. This article is an open access article distributed under the terms and conditions of the Creative Commons Attribution (CC BY) license (<https://creativecommons.org/licenses/by/4.0/>).

## 1. Introduction

Self-powered sensors are currently an emerging field of research, and researchers are showing a growing interest in triboelectric sensors. Because of their versatility and the availability of a range of materials, triboelectric nanogenerators (TENGs) occupy a significant position in self-powered sensing applications [1–4]. Typical sensing systems possess some considerable drawbacks when utilized in real-time applications, including material selectivity, stability, complex circuitry, bulky sizes and high costs [5–7]. The invention of a TENG by the group led by Z. L. Wang presented a unique contribution in the development of self-powered sensing systems [8]. The TENG uses the technology of scavenging electrical energy via the production of a static charge caused by the friction of the surfaces of two active tribo layers; moreover, through an induction effect that occurs when charges are produced on the surfaces of the electrodes, they become dynamic and produce an electrical output [8–11]. The TENG is capable of scavenging electrical energy from mechanical energy, but, thus far, it has been observed that the output power is very low in TENGs [12–14]. Therefore, in parallel to the research seeking to enhance the output power, increasing research has been conducted on high-voltage applications and self-powered sensing applications using TENGs [15–19]. A range of versatile self-powered triboelectric sensors have been designed to date, where the sensing capabilities have been shaped through device engineering, introducing new materials, preparing composite materials and using piezo materials for hybrid nanogenerators [20–23]. A high-dielectric-constant material is a desirable choice for the development of a highly efficient TENG,

as a high dielectric constant helps to produce a larger number of triboelectric charges due to triboelectrification [24,25]. Air possesses a certain dielectric constant, and, in most cases, the effects of charged air are ignored when developing TENGs [26,27]. The charged air is passed on in each contact–separation process. The flow of charged air diminishes the output performance of TENGs [26,27]. Herein, we report a triboelectric pressure sensor using an air-trapped pad with a laser-induced graphene (LIG) electrode. LIG has enabled breakthroughs in research and has attracted attention in recent years in the field of TENGs due to its excellent output performance and multiple real-time self-powered sensing applications [14,28–30]. We have seen a great deal of research on electrode materials for TENGs, where the very costly and high-end deposition or growth of electrode materials has been reported, such as the vacuum deposition technique and chemical vapor deposition (CVD). On the other hand, metal adhesion on PI films is poor due to the effect of the adhesive material [31,32]. The formation of LIG on the surface of a good triboelectric material provides an alternative durable material in the field of TENGs as it possesses a highly conductive electrode with a high-end tribo nature [14]. We have fabricated LIG using a CO<sub>2</sub> laser on a polyimide (PI) film, as reported previously [14]. In this report, we also describe our research using a PI film where a CO<sub>2</sub> laser was irradiated on one of its surfaces and we developed an array of electrodes. The advantage of using a PI film to produce LIG for a TENG is that the film of one material acts as both the triboelectric layer and conducting electrode, respectively. The PI layer acts as a good tribo-negative material and the LIG acts as a conducting electrode, which makes it attractive for real-time triboelectric sensing applications. In our study, we have developed a mask-generated air-trapped circular pad using silicone rubber. The flat surface of the PI film and the mask-generated padded film of silicone rubber are attached together using tape in such a way that prevents air leaks. The air-trapped padded area of 1.13 cm<sup>2</sup> with a height of 0.6 mm is the key characteristic of our device air-trapped padded sensor (ATPS). A light touch on the air-trapped pad can cause contact–separation between the silicone rubber (SR) and PI film and produces triboelectrification and, hence, an electric output voltage. The device engineering along with the use of trapped air as a dielectric medium makes the ATPS highly sensitive over very low amplitudes under a range of pressure levels. We show how the trapped air impacts the sensitivity of the device by comparing the voltage output when the air in the pad is passed in each stage of contact and separation. A device size of 20 × 15 × 1 mm<sup>3</sup>, having an air-trapped padded area of 1.13 cm<sup>2</sup>, delivers a peak-to-peak output voltage of 32 V, a current of 1.2 μA and maximum power of 15.8 μW. We demonstrate that our device is potentially suitable for real-time multipurpose healthcare sensing applications.

## 2. Materials and Methods

### 2.1. Preparation of LIG Film Using PI Film

Using a CO<sub>2</sub> laser engraving system in a normal air environment, a CO<sub>2</sub> laser was continuously irradiated on the specific area of the PI film. The array of electrodes on the PI film was designed using computer-aided design (CAD). Scanning power of irradiation of 6 W was used and the velocity of scanning was 450 mm s<sup>−1</sup>. The gap between scan steps was 0.025 mm. The typical process time of CO<sub>2</sub> laser irradiation was approximately 7 min for an LIG film having a size of 50 × 50 mm<sup>2</sup>. A schematic of the fabrication of the LIG is shown in Figure 1.

### 2.2. Preparation of Circular Padded Film of Silicone Rubber

A thick paper was taken and the upper surface was covered using double-sided tape. A circular aluminum plate with a 0.6 mm thickness and a 1.2 cm diameter was placed in the middle of the paper. At each side of the circular plate, at a distance of 5 mm, four straight wires, 1 mm in diameter and 1.2 cm long, were placed at a distance of 2 mm from each other (Figure 2a). Part A and part B of the silicone rubber were taken in a 1:1 mass ratio and stirred; finally, the mold was drop-cast on the mask-designed thick paper (Figure 2b).

Finally, after 1 h, the dried silicone rubber film was removed from the paper and, hence, we obtained a padded film with a friction enhancing layer, as shown in Figure 2c.

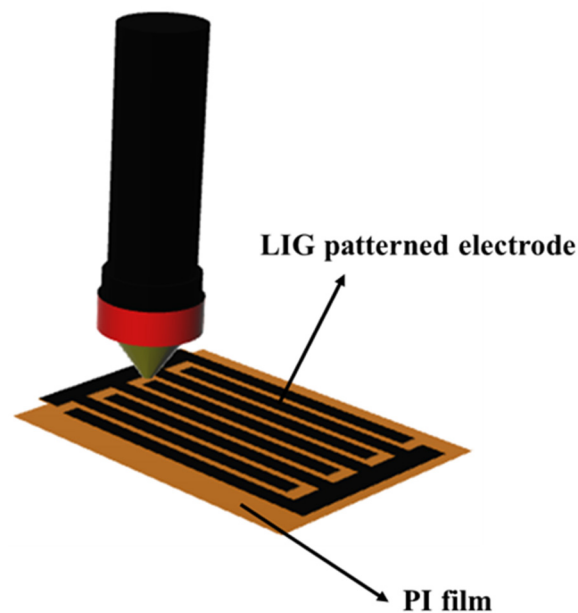


**Figure 1.** Schematic of the fabrication method of LIG array on PI film.

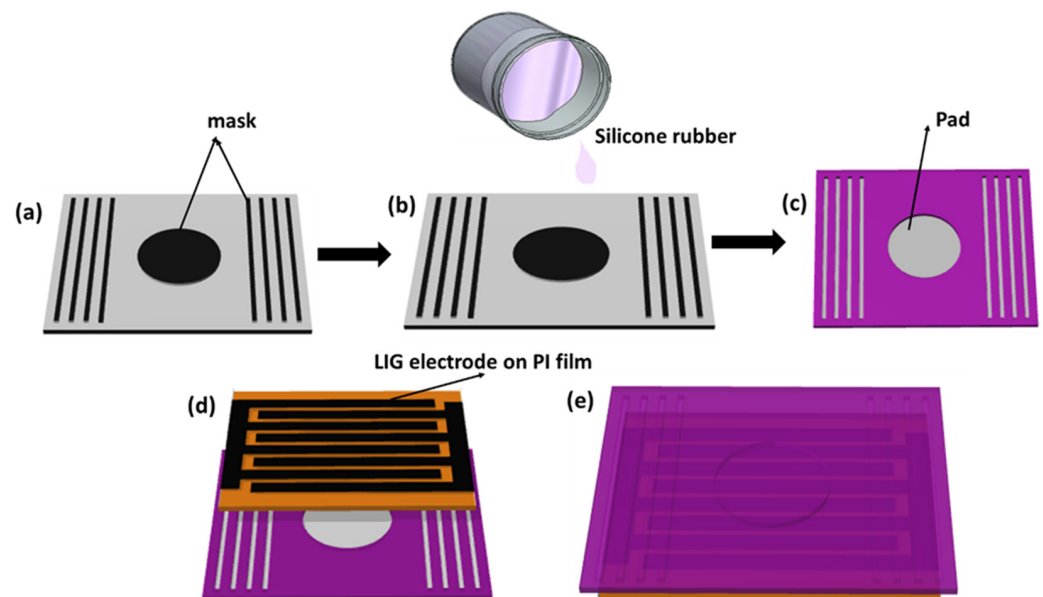


**Figure 2.** The schematic of the fabrication of ATPS. (a) The mask placed on the thick paper to create a pad and some frictional layers. (b) Pouring of silicone rubber onto the masked paper. (c) Padded silicone rubber film. (d) LIG electrode with a PI film and a film of padded silicone rubber vertically attached. (e) Schematic of the air-locked ATPS in working condition.

### 2.3. Characterization and Electrical Output Measurements

Field emission scanning electron microscopy (FESEM) and colored energy-dispersive X-ray spectroscopy (EDS) images of an intrinsic silicone foam were taken using an FEI device (Apreo S HiVac, Thermo Fisher Scientific, Waltham, MA, USA), and Fourier transform infrared spectrometry (FT-IR) analysis was performed using a Bruker Optik GmbH device (Vertex-70V/Hyperion 3000, Keyence, Tampa, FL, USA).

The electrical output signal was measured using a digital oscilloscope (TBS 2202 B, Tektronix, Beaverton, OR, USA), a high-voltage probe (P5100 A, Tektronix, USA) and a current amplifier (DLPCA-200, Femto, Berlin, Germany).

#### 2.4. Fabrication of Air-Trapped Padded Sensor (ATPS)

The padded films of silicone rubber and LIG were vertically attached together using tape in such a way that no air leakage took place, as shown in Figure 2d,e. The resultant thickness of the ATPS was 1 mm.

### 3. Results and Discussion

A number of approaches to enhancing the output voltage of TENGs have been devised to date, using popular tribo-negative polymers such as polydimethylsiloxane (PDMS), polyvinylidene fluoride (PVDF), nylon and silicone rubber [2,9,33–35]. Various triboelectric sensors focusing on the use of dielectric materials have been reported to date [36,37]. In our study, we utilized air, which possesses a dielectric constant of 1, as an enhancer of the triboelectric output. The ultrathin and ultrasensitive triboelectric sensor, the ATPS, was fabricated using LIG and SR. A schematic of the fabrication of the LIG film is shown in Figure 1, and the fabrication process is described in the Materials and Methods. The thickness of the LIG was 0.25 mm. Our ATPS is a single-electrode system, with the only electrical connection being to the LIG.

The trapping of air was accomplished by utilizing a pad created with SR. The scheme of the fabrication of the pad is described in the Materials and Methods section, with corresponding figures provided in Figure 2a–c. The vertical attachment between the PI and SR is depicted in Figure 2d. The trapping was achieved by using a silicone rubber pad and PI film. During the fabrication of the device, we took care to ensure that there was no air leakage in the ATPS, as shown in Figure 2e. The characterization for SR was conducted through SEM, FTIR and color mapping energy-dispersive X-ray spectroscopy (EDS). For the PI film, color mapping EDS and SEM were performed. To observe the nature of the surfaces of the grown LIG on the PI film, we took SEM images of the LIG. We characterized the SR and PI films by EDS, as shown in Figure 2a,b, respectively. We can observe from the EDS results that the silicone rubber contained the elements carbon (C), oxygen (O) and silicon (Si), as shown in Figure 3a. From the FTIR spectra, we can see the presence of hydrogen-associated bonds, indicating the presence of hydrogen (H) in the SR. However, it is important to note that hydrogen was not detectable in EDS. On the other hand, the PI contained nitrogen (N), carbon (C), oxygen (O), silicon (Si) and hydrogen (H), as shown in Figure 3b. Notably, hydrogen was not detected by EDS. The surface morphology of the LIG, PI and SR was examined using scanning electron microscopy (SEM), as shown in Figure 3c–e, respectively.

We can observe that the electrode grown under laser irradiation on PI is porous and exhibits a continuous nature, as shown in Figure 3c. The SEM images reveal that the surface of the SR is rougher than surface of the PI, which is desirable in TENGs as it helps to achieve higher friction when they come into contact with each other, as shown in Figure 3d,e. We conducted Fourier transform infrared spectroscopy (FTIR) analysis on the SR to identify the functional groups present. The characteristic peaks in the FTIR spectrum reveal the presence of all bonds required to form silicone rubber, as illustrated in Figure 3f. The characteristic peak at  $790\text{ cm}^{-1}$  corresponds to the presence of the  $\text{Si}-(\text{CH}_3)_2$  group, the peak at  $1010\text{ cm}^{-1}$  corresponds to the main chain of the Si-O-Si bond, the peak at  $1260\text{ cm}^{-1}$  corresponds to the Si-CH<sub>3</sub> group, and the peak at  $2960\text{ cm}^{-1}$  corresponds to the vibrations of the C-H bond in the CH<sub>3</sub> group [38].

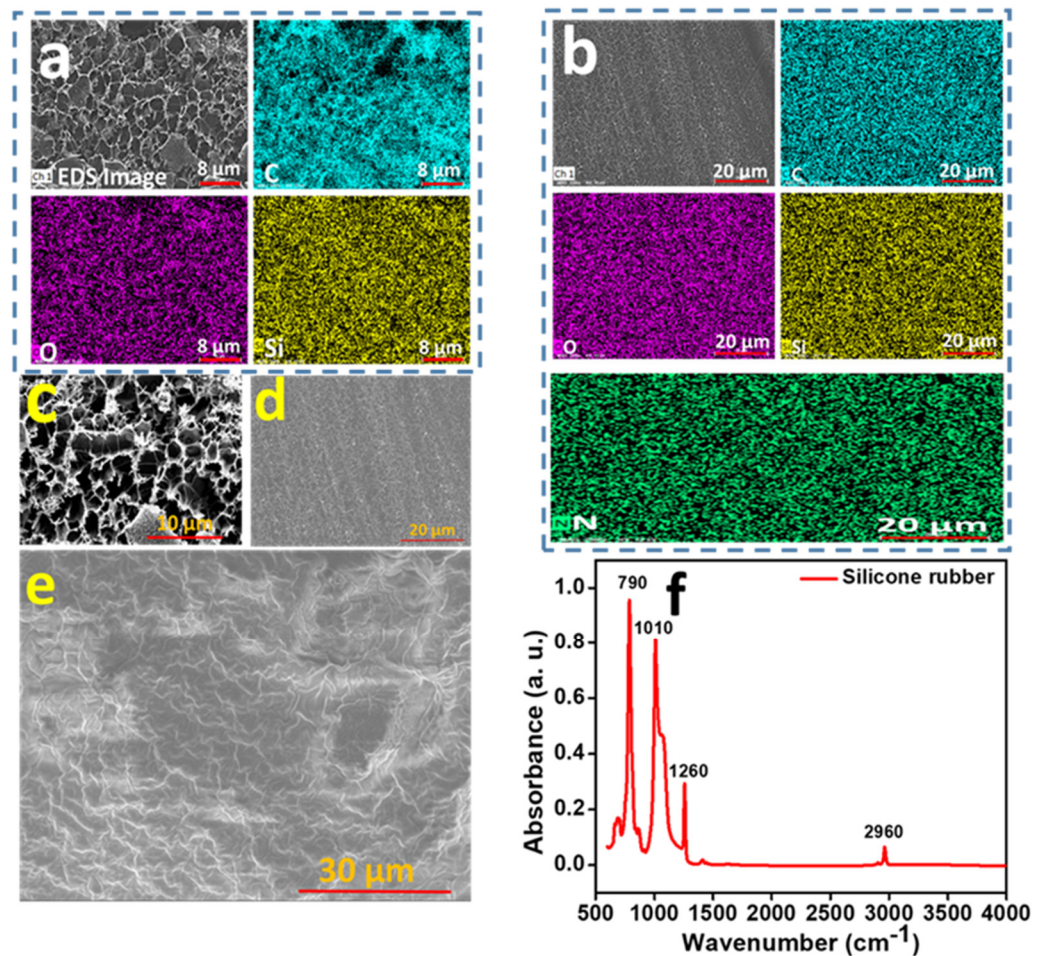


**Figure 3.** (a) EDS of silicone rubber. (b) EDS of PI film. (c) SEM of LIG. (d) SEM of PI film. (e) SEM of the film of silicone rubber. (f) FTIR spectra for silicone rubber.

The electrical output characteristics were determined by applying force through tapping the air-trapped pad with a finger. The sensor was a single-electrode circuitry system, where the only connection was to the LIG electrode, and effective triboelectrification took place in the air-trapped pad. The single-electrode system makes it less complex, lightweight and user-friendly, enabling the fabrication of a leakage-free sensor. Frictional layers on both sides of the air pad were developed, capable of participating in the triboelectrification process when the device undergoes twisting or stretching, as indicated by the black lines in Figure 2a,b. The combination of the air pad and frictional layers on both sides makes the sensor highly responsive to various externally applied forces generated by different body parts. Therefore, the ATPS shows potential application in the field of healthcare sensing. Except for the air-trapped pad, which has a gap of 0.6 mm, the other parts of the silicone rubber film are fully attached to the PI film. This ensures that the ATPS is fully airtight. To verify the uniqueness of the trapped-air pad and the frictional layers, we compared the output from the three devices, as shown in Figure 4a–c. We applied external tapping both on the outside and inside of the pad, measured the voltage and current and compared the effectiveness of the trapped air inside the pad. We applied an external force to the outside of the pad, as shown in Figure 4a. A very low output voltage of 6 V and a current of 0.12  $\mu\text{A}$  resulted from the finger effect on the SR film. Since there is no gap between the SR and PI film, no contact–separation occurs between the PI and SR film, as shown in Figure 4a. When tapping is applied to the air-trapped pad, the output voltage dramatically increases fivefold to 32 V, and the current increases tenfold to 1.2  $\mu\text{A}$ , as shown in Figure 4b. The increase in output voltage is attributed to the contact–separation and the trapped charged air in the pad. Due to triboelectrification, the trapped air becomes charged simultaneously

with the generation of static charges on the surfaces of the PI and SR films, contributing to the higher electrical output. The effect of charged air was validated by creating a hole in the pad and measuring the output voltage and current, as shown in Figure 4c. The hole in the pad allows air to pass from the inside to the outside during contact–separation, resulting in a significant drop in the output voltage and current, with average values of 20 V and 0.8  $\mu\text{A}$ , respectively. This suggests that the charged and trapped air helps to enhance the electrical output in our device. By utilizing trapped air as a dielectric medium, we fabricated the ATPS, which generates a higher current of 1.2  $\mu\text{A}$ , corresponding to the current density of  $10.6 \text{ mA}\cdot\text{m}^{-2}$ . Therefore, we observed ultra-sensitive output characteristics in the sensing application.

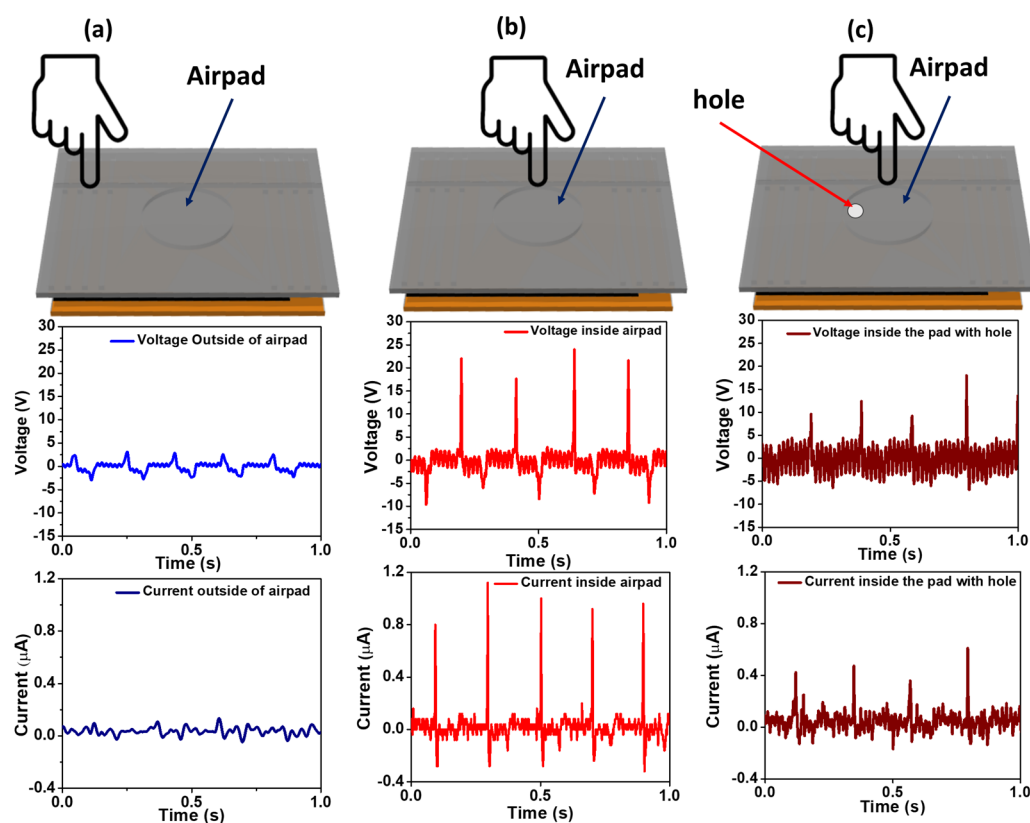


**Figure 4.** Output voltage and current while tapping. (a) Outside the trapped air pad. (b) On the trapped air pad. (c) On the air pad with a hole.

We studied the electrical characteristics of the ATPS exclusively using the air-trapped padded device, as it provided a higher electrical output compared to the pad with a hole, as shown in Figure 4b,c. However, we also measured the amount of transferred charge at each pressing time, as shown in Figure 5a. By integrating a positive peak of the current pulse, we can observe that the transferred charge for each strike is approximately 0.0027  $\mu\text{C}$ , corresponding to a charge density of  $23.9 \mu\text{C m}^{-2}$ .

Similarly, when measuring the output voltage across the external resistance, we observed that the output voltage changed linearly with the resistance. It increased with the increase in the value of resistance and became saturated at 32 V when the resistance reached  $1\text{G}\Omega$ , as shown in Figure 5b. The high value of  $1\text{G}\Omega$  mimics an open-circuit voltage, resulting in an output voltage of 32 V, similar to the open-circuit output voltage shown in Figure 4b. It is necessary to measure the output power of a device under its working conditions. The output power of the ATPS was checked, and we obtained a maximum of 15.8  $\mu\text{W}$  at a resistance value of  $10 \text{ M}\Omega$ , as shown in Figure 5b. Therefore, we achieved the maximum power density of  $139.8 \text{ mW m}^{-2}$  at a resistance level of  $10 \text{ M}\Omega$ . At this level of resistance, the device becomes highly electrically sensitive, as it can deliver higher output

even under very low amplitudes of external force. Our ATPS is highly sensitive to a versatile range of low-pressure amplitudes, and we have demonstrated its potential application in healthcare sensing. To make our device compatible for real-time applications in the field of healthcare sensing, we sought to develop a highly flexible, twistable and robust sensor. To achieve this, we replaced the LIG with conductive carbon tape without compromising the air-trapped pad. The conducting carbon tape serves as both the triboelectric material and the conducting electrode. We attached carbon tape with dimensions of  $20 \times 15 \text{ mm}^2$  to the padded film of SR, ensuring no air leakage. The only electrode was connected to the conductive carbon tape. The resultant device was applied in multipurpose healthcare sensing applications, as depicted in Figure 6.

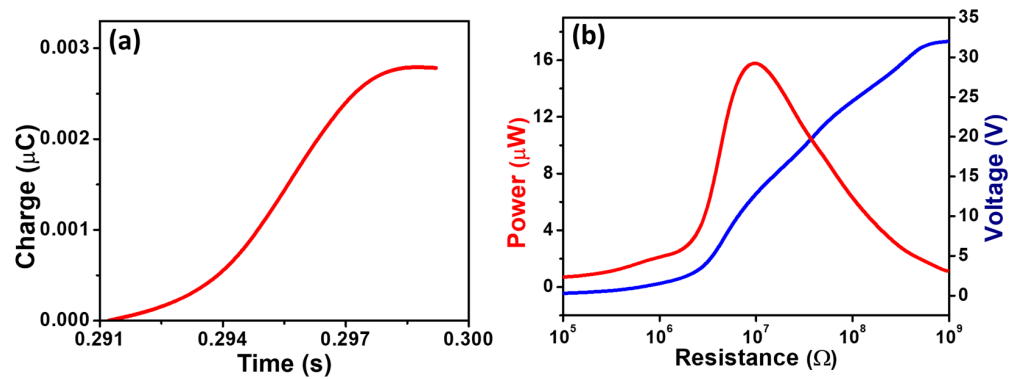


Figure 5. (a) Plot for amount of transferred charge at each pressing time. (b) The output power and the variation in the output voltage under different levels of external resistance.

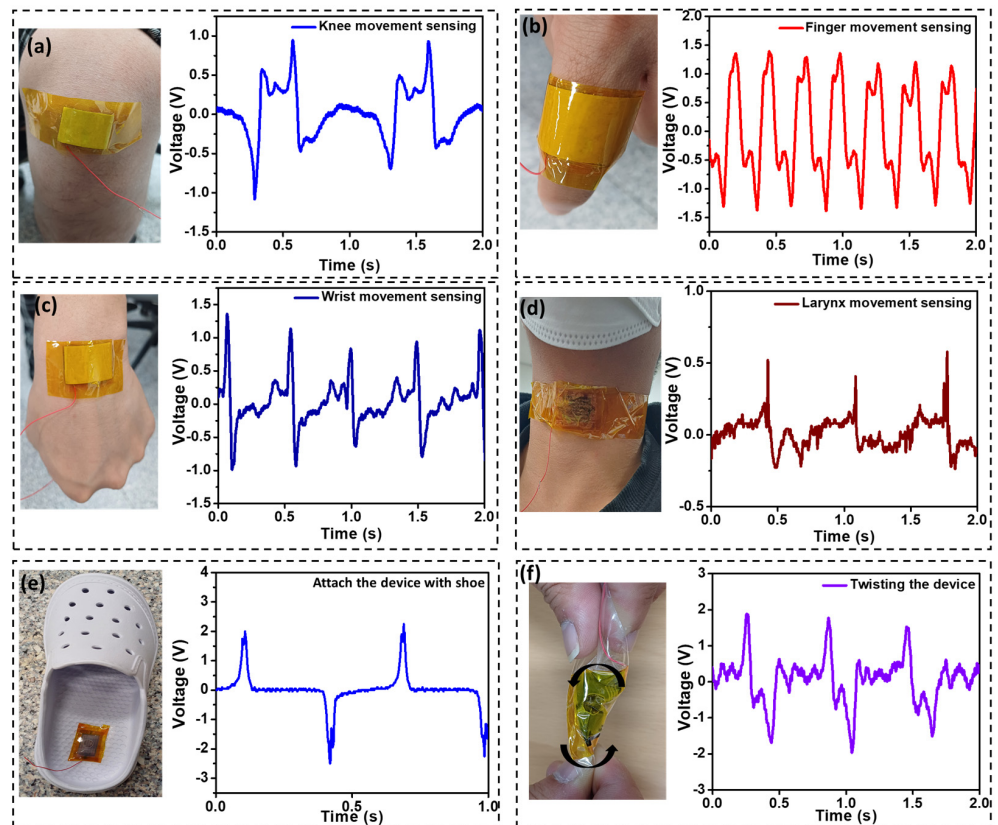


Figure 6. Multipurpose applications of ATPS. (a) Knee movement sensing. (b) Finger movement sensing. (c) Wrist movement sensing. (d) Larynx movement sensing. (e) Step recording. (f) Voltage corresponding to twisting of the device, where the arrow shows the direction of the twist.

We have provided a table comparing the output performance of triboelectric sensors reported previously with that developed in our research work, as shown in Table 1. This provides an insight into the potential real-time application of our sensor, the ATPS [39–46].

**Table 1.** A comparative study of reported healthcare sensors with our device, the ATPS.

Ref. Work	Type	Materials Used	Size	Mode of Operation	Max. Current	Power Density
[39]	Sleep sensor	APLF–Cu	1.8 cm <sup>2</sup>	Contact–separation	0.9 μA	120 mW/m <sup>2</sup>
[40]	Motion sensor	ABS–Cu	-	Contact–separation	0.26 μA	0.22 μW/cm <sup>3</sup>
[41]	Cardiovascular sensor	FEP–PET	1.5 × 3 cm <sup>2</sup>	Contact–separation	-	23 μW/m <sup>2</sup>
[42]	Coronary heart disease sensor	Kapton–Cu	20 × 10 mm <sup>2</sup>	Contact–separation	2.73 μA	-
[43]	Tactile sensor	Ionogel–PDMS	2 × 1.5 cm <sup>2</sup>	Contact–separation	2.3 nA	-
[44]	Touch sensor	P(VDF-TrFE)–PDMS	-	Contact–separation	-	46.7 μW/cm <sup>2</sup>
[45]	Respiratory sensor	PTFE–Al	3 × 2 × 0.1 cm <sup>3</sup>	Contact–separation	4 μA	-
[46]	Pulse sensor	PET	40 × 20 mm <sup>2</sup>	Single-electrode mode	5.4 nA	-
<b>Our work</b>	<b>Multipurpose pressure sensor</b>	<b>LIG–silicone rubber</b>	<b>1.13 cm<sup>2</sup></b>	<b>Contact–separation</b>	<b>1.2 μA</b>	<b>139.8 mW/m<sup>2</sup></b>

We attached our sensor to the knee, and, with each small movement, the sensor recorded the corresponding signal. When the knee is folded, the SR and carbon tape come into contact, resulting in a positive peak of 0.95 V. Similarly, when the leg straightens, separation occurs between the films, producing a negative pulse of 0.45 V, as shown in Figure 6a. This indicates that our sensor can be utilized to monitor the up–down cycle during knee exercises based on the peak count. The position of the ATPS’ attachment is crucial; the most intense peaks were obtained when the device was attached at the knee joint. The use of other positions on the knee may disrupt the efficiency of the ATPS, as proper contact–separation may not occur, leading to discontinuous peak counts for each folding and straightening movement of the leg. In the case of conscious patients recovering from an illness, finger movement is often one of the first signs of recovery. For this reason, we attached our sensor to the middle portion of a finger, as shown in Figure 6b. Here, when the finger is folded down, contact occurs between the SR film and the carbon conductive tape, resulting in a positive peak with a value of 1.55 V. Similarly, when the finger is in a straight position, the films separate, and a corresponding negative peak of 1.35 V is observed; see Figure 6b. We also registered wrist movement by attaching the sensor to the wrist of a hand, as shown in Figure 6c. A straight-down or angled move causes contact, while an upward move causes separation between the two films. Each action generates a positive and negative voltage peak, with values of 1.1 V and 0.9 V, respectively. Optimal positioning at the wrist junction enhances the signal output by improving the contact and separation. The larynx is a vital organ for speech and breathing cycles [47]. Patient recovery often involves attempting to talk, causing the larynx to move or vibrate. To capture this movement, we attached our device to the larynx, as shown in Figure 6d. During speech, the larynx movement results in contact–separation between the two films in the pad, producing positive and negative peaks of 0.52 V and 0.25 V, respectively. These signals were recorded in the output. The sensing of larynx movement is a crucial application in the field of triboelectric sensors. In modern healthcare monitoring, physical exercise plays a significant role. Gait movement is particularly important, as various forms of walking and running have positive impacts on the human body. To incorporate our ATPS device into gait sensing, we attached the sensor to a shoe. With each press and release of the heel, the device registered positive and negative peaks with values of 2 V and 2.5 V, respectively; see Figure 6e. The device enables step counting, making it useful for health monitoring during running or walking. Finally, we tested the robustness of the device by twisting it, as shown in Figure 6f. Changes in the direction of the twist can generate corresponding positive and negative voltage peaks. In each application, optimal sensing results were observed when the device was properly positioned on the corresponding body

parts, allowing for full contact–separation between the two films. While we demonstrated the electrical characteristics of the ATPS by manually applying force through tapping the air pad, the stability of the sensor over a large number of cycles was not explored. However, since silicone rubber and PI are highly stable in ambient conditions for prolonged periods, we anticipate that the ATPS will deliver a stable output over an extended duration. The significance of the trapped air in the pad, leading to a higher electric output, and the broad range of applications in healthcare sensing make the ATPS crucial for real-time biomedical applications.

#### 4. Conclusions

We fabricated a triboelectric sensor using an air-trapped pad with LIG. The novelty of the device fabrication, utilizing air as a dielectric layer, offers opportunities for research in the field of triboelectric nanogenerators. In our work, we demonstrated the efficacy of trapped air as an effective dielectric layer by comparing it with a normal padded device that had a hole. We highlighted the difference in output between the two devices. The ATPS generated an output voltage of 32 V and a power density of 139.8 mW m<sup>−2</sup>. With a device size of 20 × 15 × 1 mm<sup>3</sup> and effective padding area spacing of only 0.6 mm, it can be utilized in a wide range of pressure sensing applications. LIG plays a crucial role in keeping the device thin, as the array of electrodes was grown on the surface of a PI film using CO<sub>2</sub> laser irradiation. The significance of the charged air, its role in creating a highly sensitive sensor and the versatility in healthcare sensing applications make our device attractive for potential applications in the field of triboelectric nanogenerators.

**Author Contributions:** Conceptualization, methodology, experiment, validation, writing—original draft, writing—review and editing, T.K.; methodology, writing—review and editing, D.H.; validation, resources, writing—review and editing, J.S.; supervision, investigation, funding acquisition, validation, resources, writing—review and editing, S.K. and J.P. All authors have read and agreed to the published version of the manuscript.

**Funding:** This research was funded by the Post.-Doc. scholarship program of KOREATECH, “Regional Innovation Strategy (RIS)”, through the National Research Foundation of Korea (NRF) funded by the Ministry of Education (MOE) (2021RIS-004); the Next-Generation Intelligence Semiconductor Foundation funded by the Ministry of the Trade, Industry and Energy (20023549); and the Korea Institute for the Advancement of Technology (KIAT) funded by the Korea Government (MOTIE) through the “Competency Development Program for Industry Specialist” (P0008458).

**Institutional Review Board Statement:** Not applicable.

**Data Availability Statement:** The data are available on reasonable request from the corresponding author.

**Acknowledgments:** We acknowledge the Post.-Doc. scholarship program of KOREATECH and the Education Common Equipment Center for allowing us the use of their scanning electron microscopy, Fourier transform infrared spectroscopy and energy-dispersive X-ray spectroscopy facilities.

**Conflicts of Interest:** The authors declare no conflict of interest.

#### References

1. Wang, S.; Lin, L.; Wang, Z.L. Triboelectric nanogenerators as self-powered active sensors. *Nano Energy* **2015**, *11*, 436–462. [[CrossRef](#)]
2. Wang, Z.L. Triboelectric Nanogenerator (TENG)—Sparking an Energy and Sensor Revolution. *Adv. Energy Mater.* **2020**, *10*, 2000137. [[CrossRef](#)]
3. Tao, J.; Bao, R.; Wang, X.; Peng, Y.; Li, J.; Fu, S.; Pan, C.; Wang, Z.L. Self-Powered Tactile Sensor Array Systems Based on the Triboelectric Effect. *Adv. Funct. Mater.* **2019**, *29*, 1806379. [[CrossRef](#)]
4. Jiang, J.; Sun, X.; Wen, Z. Perspectives of Triboelectric Sensors for Internet of Healthcare. *Adv. Sens. Res.* **2022**, *1*, 2200011. [[CrossRef](#)]
5. Korotcenkov, G.; Cho, B.K. Ozone measuring: What can limit the application of SnO<sub>2</sub>-based gas sensors? *Sens. Actuators B* **2012**, *161*, 28–44. [[CrossRef](#)]

6. Suriano, D. A Portable Air Quality Monitoring Unit and a Modular, Flexible Tool for on-Field Evaluation and Calibration of Low-Cost Gas Sensors. *HardwareX* **2021**, *9*, e00198. [[CrossRef](#)] [[PubMed](#)]
7. Ren, K.; Huang, L.; Yue, S.; Lu, S.; Liu, K.; Azam, M.; Wang, Z.; Wei, Z.; Qu, S.; Wang, Z. Turning a disadvantage into an advantage: Synthesizing high-quality organometallic halide perovskite nanosheet arrays for humidity sensors. *J. Mater. Chem. C* **2017**, *5*, 2504–2508. [[CrossRef](#)]
8. Fan, F.-R.; Tian, Z.-Q.; Wang, Z.L. Flexible triboelectric generator. *Nano Energy* **2012**, *1*, 328–334. [[CrossRef](#)]
9. Kamilya, T.; Sarkar, P.K.; Acharya, S. Unveiling Peritoneum Membrane for a Robust Triboelectric Nanogenerator. *ACS Omega* **2019**, *4*, 17684–17690. [[CrossRef](#)]
10. Sarkar, P.K.; Kamilya, T.; Acharya, S. Introduction of Triboelectric Positive Bioplastic for Powering Portable Electronics and Self-Powered Gait Sensor. *ACS Appl. Energy Mater.* **2019**, *2*, 5507–5514. [[CrossRef](#)]
11. Wang, Z.L. Triboelectric Nanogenerators as New Energy Technology for Self-Powered Systems and as Active Mechanical and Chemical Sensors. *ACS Nano* **2013**, *7*, 9533–9557. [[CrossRef](#)]
12. Wang, N.; Wang, X.X.; Yan, K.; Song, W.; Fan, Z.; Yu, M.; Long, Y.Z. Anisotropic Triboelectric Nanogenerator Based on Ordered Electrospinning. *ACS Appl. Mater. Interfaces* **2020**, *12*, 46205–46211. [[CrossRef](#)]
13. Pan, R.; Xuan, W.; Chen, J.; Dong, S.; Jin, H.; Wang, X.; Li, H.; Luo, J. Fully biodegradable triboelectric nanogenerators based on electrospun polylactic acid and nanostructured gelatin films. *Nano Energy* **2018**, *45*, 193–202. [[CrossRef](#)]
14. Stanford, M.G.; Li, J.T.; Chyan, Y.; Wang, Z.; Wang, W.; Tour, J.M. Laser-Induced Graphene Triboelectric Nanogenerators. *ACS Nano* **2019**, *13*, 7166–7174. [[CrossRef](#)]
15. Lei, R.; Shi, Y.; Ding, Y.; Nie, J.; Li, S.; Wang, F.; Zhai, H.; Chen, X.; Wang, Z.L. Sustainable high-voltage source based on triboelectric nanogenerator with a charge accumulation strategy. *Energy Environ. Sci.* **2020**, *13*, 2178–2190. [[CrossRef](#)]
16. Bai, Y.; Feng, H.; Li, Z. Theory and applications of high-voltage triboelectric nanogenerators. *Cell Rep. Phys. Sci.* **2022**, *3*, 101108. [[CrossRef](#)]
17. Cao, X.; Jie, Y.; Wang, N.; Wang, Z.L. Triboelectric nanogenerators driven self-powered electrochemical processes for energy and environmental science. *Adv. Energy Mater.* **2016**, *6*, 1600665. [[CrossRef](#)]
18. Zou, H.-X.; Zhao, L.-C.; Wang, Q.; Gao, Q.-H.; Yan, G.; Wei, K.-X.; Zhang, W.-M. A self-regulation strategy for triboelectric nanogenerator and self-powered wind-speed sensor. *Nano Energy* **2022**, *95*, 106990. [[CrossRef](#)]
19. Nazar, A.M.; Narazaki, Y.; Rayegani, A.; Sardo, F.R. Recent progress of triboelectric nanogenerators as self-powered sensors in transportation engineering. *Measurement* **2022**, *203*, 112010. [[CrossRef](#)]
20. Khandelwal, G.; Chandrasekhar, A.; Raj, N.P.M.J.; Kim, S.-J. Metal-Organic Framework: A Novel Material for Triboelectric Nanogenerator-Based Self-Powered Sensors and Systems. *Adv. Energy Mater.* **2019**, *9*, 1803581. [[CrossRef](#)]
21. Liu, H.Y.; Wang, H.; Lyu, Y.; He, C.F.; Liu, Z.H. A novel triboelectric nanogenerator based on carbon fiber reinforced composite lamina and as a self-powered displacement sensor. *Microelectron. Eng.* **2020**, *224*, 9. [[CrossRef](#)]
22. Han, Z.; Jiao, P.; Zhu, Z. Combination of Piezoelectric and Triboelectric Devices for Robotic Self-Powered Sensors. *Micromachines* **2021**, *12*, 813. [[CrossRef](#)]
23. Zhang, J.; He, Y.; Boyer, C.; Kalantar-Zadeh, K.; Peng, S.; Chu, D.; Wang, C.H. Recent Developments of Hybrid Piezo–Triboelectric Nanogenerators for Flexible Sensors and Energy Harvesters. *Nanoscale Adv.* **2021**, *3*, 5465–5486. [[CrossRef](#)]
24. Lee, J.W.; Cho, H.J.; Chun, J.; Kim, K.N.; Kim, S.; Ahn, C.W.; Kim, I.W.; Kim, J.; Kim, S.; Yang, C.; et al. Robust nanogenerators based on graft copolymers via control of dielectrics for remarkable output power enhancement. *Sci. Adv.* **2017**, *3*, e1602902. [[CrossRef](#)]
25. Shao, Y.; Feng, C.; Deng, B.; Yin, B.; Yang, M. Facile method to enhance output performance of bacterial cellulose nanofiber based triboelectric nanogenerator by controlling micro-nano structure and dielectric constant. *Nano Energy* **2019**, *62*, 620–627. [[CrossRef](#)]
26. Zi, Y.; Wu, C.; Ding, W.; Wang, Z.L. Maximized Effective Energy Output of Contact-Separation-Triggered Triboelectric Nanogenerators as Limited by Air Breakdown. *Adv. Funct. Mater.* **2017**, *27*, 1700049. [[CrossRef](#)]
27. Jiang, C.; Dai, K.; Yi, F.; Han, Y.; Wang, X.; You, Z. Optimization of triboelectric nanogenerator load characteristics considering the air breakdown effect. *Nano Energy* **2018**, *53*, 706–715. [[CrossRef](#)]
28. Chen, Y.; Xie, B.; Long, J.; Kuang, Y.; Chen, X.; Hou, M.; Gao, J.; Zhou, S.; Fan, B.; He, Y.; et al. Interfacial laser-induced graphene enabling high-performance liquid–solid triboelectric nanogenerator. *Adv. Mater.* **2021**, *33*, 2104290. [[CrossRef](#)]
29. Zou, Y.; Zhong, M.; Li, S.; Qing, Z.; Xing, X.; Gong, G.; Yan, R.; Qin, W.; Shen, J.; Zhang, H.; et al. Flexible Wearable Strain Sensors Based on Laser-Induced Graphene for Monitoring Human Physiological Signals. *Polymers* **2023**, *15*, 3553. [[CrossRef](#)]
30. Zhao, P.; Bhattacharya, G.; Fishlock, S.J.; Guy, J.G.M.; Kumar, A.; Tsonos, C.; Yu, Z.; Raj, S.; McLaughlin, J.A.; Luo, J.; et al. Replacing the metal electrodes in triboelectric nanogenerators: High-performance laser-induced graphene electrodes. *Nano Energy* **2020**, *75*, 104958. [[CrossRef](#)]
31. Chu, H.; Jang, H.; Lee, Y.; Chae, Y.; Ahn, J.H. Conformal, graphene-based triboelectric nanogenerator for self-powered wearable electronics. *Nano Energy* **2016**, *27*, 298–305. [[CrossRef](#)]
32. Inagaki, N.; Tasaka, S.; Masumoto, M. Improved adhesion between kapton film and copper metal by plasma graft polymerization of vinylimidazole. *Macromolecules* **1996**, *29*, 1642–1648. [[CrossRef](#)]
33. Xiao, T.X.; Jiang, T.; Zhu, J.X.; Liang, X.; Xu, L.; Shao, J.J.; Zhang, C.L.; Wang, J.; Wang, Z.L. Silicone-based triboelectric nanogenerator for water wave energy harvesting. *ACS Appl. Mater. Interfaces* **2018**, *10*, 3616–3623. [[CrossRef](#)]

34. Vu, D.L.; Le, C.D.; Ahn, K.K. Polyvinylidene Fluoride Surface Polarization Enhancement for Liquid-Solid Triboelectric Nanogenerator and Its Application. *Polymers* **2022**, *14*, 960. [[CrossRef](#)]
35. Choi, Y.S.; Jing, Q.; Datta, A.; Boughey, C.; Kar-Narayan, S. A Triboelectric Generator Based on Self-Poled Nylon-11 Nanowires Fabricated by Gas-Flow Assisted Template Wetting. *Energy Environ. Sci.* **2017**, *10*, 2180–2189. [[CrossRef](#)]
36. Mi, Y.; Zhao, Z.; Wu, H.; Lu, Y.; Wang, N. Porous Polymer Materials in Triboelectric Nanogenerators: A Review. *Polymers* **2023**, *15*, 4383. [[CrossRef](#)]
37. Kim, D.W.; Lee, J.H.; Kim, J.K.; Jeong, U. Material Aspects of Triboelectric Energy Generation and Sensors. *NPG Asia Mater.* **2020**, *12*, 6. [[CrossRef](#)]
38. Zhang, Z.; Liang, T.; Jiang, X.; Li, C.; Yang, S.; Zhang, Y. Characterization of silicone rubber degradation under salt-fog environment with AC test voltage. *IEEE Access* **2019**, *7*, 66714.
39. Song, W.X.; Gan, B.H.; Jiang, T.; Zhang, Y.; Yu, A.F.; Yuan, H.T.; Chen, N.; Sun, C.W.; Wang, Z.L. Nanopillar Arrayed Triboelectric Nanogenerator as a Self-Powered Sensitive Sensor for a Sleep Monitoring System. *ACS Nano* **2016**, *10*, 8097–8103. [[CrossRef](#)] [[PubMed](#)]
40. Maharjan, P.; Toyabur, R.M.; Park, J.Y. A human locomotion inspired hybrid nanogenerator for wrist-wearable electronic device and sensor applications. *Nano Energy* **2018**, *46*, 383–395. [[CrossRef](#)]
41. Chen, S.; Wu, N.; Lin, S.; Duan, J.; Xu, Z.; Pan, Y.; Zhang, H.; Xu, Z.; Huang, L.; Hu, B.; et al. Hierarchical Elastomer Tuned Self-Powered Pressure Sensor for Wearable Multifunctional Cardiovascular Electronics. *Nano Energy* **2020**, *70*, 104460. [[CrossRef](#)]
42. Ouyang, H.; Tian, J.; Sun, G.; Zou, Y.; Liu, Z.; Li, H.; Zhao, L.; Shi, B.; Fan, Y.; Fan, Y. Self-Powered Pulse Sensor for Antidiastole of Cardiovascular Disease. *Adv. Mater.* **2017**, *29*, 1703456. [[CrossRef](#)] [[PubMed](#)]
43. Zhao, G.; Zhang, Y.; Shi, N.; Liu, Z.; Zhang, X.; Wu, M.; Pan, C.; Liu, H.; Li, L.; Wang, Z.L. Transparent and Stretchable Triboelectric Nanogenerator for Self-Powered Tactile Sensing. *Nano Energy* **2019**, *59*, 302–310. [[CrossRef](#)]
44. Ha, M.; Lim, S.; Cho, S.; Lee, Y.; Na, S.; Baig, C.; Ko, H. Skin-Inspired Hierarchical Polymer Architectures with Gradient Stiffness for Spacer-Free, Ultrathin, and Highly Sensitive Triboelectric Sensors. *ACS Nano* **2018**, *12*, 3964–3974. [[CrossRef](#)] [[PubMed](#)]
45. Ma, Y.; Zheng, Q.; Liu, Y.; Shi, B.; Xue, X.; Ji, W.; Liu, Z.; Jin, Y.; Zou, Y.; An, Z.; et al. Self-powered, one-step, and multifunctional implantable triboelectric active sensor for real-time biomedical monitoring. *Nano Lett.* **2016**, *16*, 6042–6051. [[CrossRef](#)]
46. Cui, X.N.; Zhang, C.; Liu, W.H.; Zhang, Y.; Zhang, J.H.; Li, X.; Geng, L.; Wang, X.L. Pulse sensor based on single-electrode triboelectric nanogenerator. *Sens. Actuators A* **2018**, *280*, 326–331. [[CrossRef](#)]
47. Barlett, D. Respiratory functions of the larynx. *Physiol. Rev.* **1982**, *69*, 33–57. [[CrossRef](#)]

**Disclaimer/Publisher’s Note:** The statements, opinions and data contained in all publications are solely those of the individual author(s) and contributor(s) and not of MDPI and/or the editor(s). MDPI and/or the editor(s) disclaim responsibility for any injury to people or property resulting from any ideas, methods, instructions or products referred to in the content.